PHOTON STATISTICS OF CELESTIAL LIGHT SOURCES

A THESIS SUBMITTED FOR THE DEGREE OF

BACHELOR OF SCIENCE WITH HONOURS IN PHYSICS

WITH SPECIALISATION IN ASTROPHYSICS

YEO GUANG HUI TIMOTHY

A0072110A

SUPERVISOR: PROF CHRISTIAN KURTSIEFER

CO SUPERVISOR: A/P PHIL CHAN AIK HUI

Acknowledgements

I would like to thank my supervisors Professor Christian Kurtsiefer and Associate Professor Phil Chan Aik Hui for their academic advice and the opportunity to work with them. Very special thanks to my mentor Peng Kian for imparting his knowledge and insights over the course of the project, as well as for his continual guidance and patience. I would also like to acknowledge the research assistants and PhD students from the lab, especially Brenda, Chi Huan, Hou Shun, Kadir, Sandoko, Victor and Wilson, for their help and prompt pointers. Finally I would like to extend my heartfelt gratitude to my family and friends for their timely encouragement and support, and without whom I would not be able to complete the honours program.

To God be the glory!

Abstract

With their invention of the intensity interferometer, Hanbury Brown and Twiss conducted their famous experiments to determine the angular diameters of stars in the 1950s. Owing to the cost of expensive set-ups and limitations in the resolution of photon detectors, there has been limited progress until recent advancements in technology.

In this project, we introduce a spectral filtering process to the intensity interferometer and show that this increases the coherence time of the light source by 4 orders of magnitude to allow the photon detectors to resolve the Lorentzian profile of the second order correlation function, $g^{(2)}(\tau)$, measurement with a higher signal to noise ratio and thus increase the photon bunching signal. Our $g^{(2)}(\tau)$ measurements with a mercury discharge lamp, an arc lamp and the sun reveal strong photon bunching signals which are one order of magnitude higher than previously observed for blackbodies. We hope that such filtering techniques may help in the revival of intensity interferometry as a tool in astronomy.

Contents

Chapter 1

Introduction

1.1 Background

In the 1950s, Hanbury Brown and Twiss described a new type of interferometer known as an intensity interferometer, which could measure the angular diameter of radio-frequency radiation sources and was unaffected by atmospheric scintillations which introduced phase shifts in the wavefront[1,2]. Anticipating its potential application in the optical domain, Hanbury Brown and Twiss measured the angular diameter of Sirius, a star with light in the visible spectrum, to within 10% of the calculated angular diameter[3].

In addition, with their intensity interferometer, Hanbury Brown and Twiss demonstrated photon bunching in photon detection events, leading to the development of the theory of photon statistics and the classification of light based on the second order correlation function[4], $g^{(2)}(\tau)$.

1.2 Motivation

After the early works of Hanbury Brown and Twiss, progress in the field of intensity interferometry was limited and did not find widespread adoption in the observation of celestial objects due to the cost of expensive set-ups and limitations in the resolution of photon detectors.

While the photon bunching signal was observed with pseudo-thermal light sources, such as a laser light beam passing through a rotating ground glass[5], the signals from thermal light sources or blackbodies were flat with intensity interferometry. This was because the

coherence time related to the photon bunching signal in blackbodies was on the order of femtoseconds and the photon detectors' resolution was in the nanosecond range, resulting in the latter not being able to resolve the signal.

However, recent advancements in technology have led to photon detectors with tens of picoseconds resolution and thus, the aim of our project is to build a modified intensity interferometer which introduces a spectral filtering process to increase the coherence time of the light source, allowing the photon detectors to resolve the Lorentzian profile of the $g^{(2)}(\tau)$ measurements with a higher signal to noise ratio and so increase the photon bunching signal from blackbodies such as the sun.

In our project, the spectral filtering process will narrow the bandwidth of the sun from approximately 400nm to 2pm. This increases the coherence time of the photon bunching signal from the order of 10fs to 0.5ns and thus allows our photon detectors of 40ps resolution to resolve the Lorentzian profile of the $g^{(2)}(\tau)$ measurements and obtain a photon bunching signal with an order magnitude higher than a recent experiment conducted (refer to section 4.3).

A publication of our results is currently in preparation and will be submitted soon (arXiv: 1403.7432 [quant-ph]).

1.3 Theory

The theory covered in this section will include the interpretations and mathematics of the second order correlation function, $g^{(2)}(\tau)$, and how it relates to coherent, bunched and antibunched light.

1.3.1 Second Order Correlation Function, $g^{(2)}(\tau)$

The $g^{(2)}(\tau)$ is an intensity correlation function and can be interpreted in two ways—classically and quantum mechanically. In the classical interpretation, the $g^{(2)}(\tau)$ is defined in terms of the intensity fluctuations of incident light while in the quantum interpretation, the $g^{(2)}(\tau)$ is defined in terms of coincidences between photon counting events[6].

To understand the $g^{(2)}(\tau)$ classically, we consider a Hanbury Brown-Twiss (HBT) experiment involving the intensity interferometer[6,7] (Fig 1).

In this experiment, light from a mercury discharge lamp is sent though a 50:50 beamsplitter and is detected by two photomultipliers, PMT1 and PMT2, which generate photocurrents i_1 and i_2 respectively. The photocurrents are then passed through amplifiers to give outputs proportional to the fluctuations in the photocurrents, Δi_1 and Δi_2. The latter output is passed through a time delay generator. Lastly, the two signals are sent into a multiplier-integrator unit which multiplies the signals and averages them over the time period of measurement. The output signal from the multiplier-integrator unit is proportional to $\langle \Delta i_1(t) \Delta i_2(t+\tau) \rangle$, where τ is the delay introduced by the delay generator, and the angled brackets indicate time average.

Since photocurrents are proportional to light intensities, the quantity $\langle \Delta i_1(t) \Delta i_2(t+\tau) \rangle$ is proportional to $\langle \Delta I_1(t) \Delta I_2(t+\tau) \rangle$, where $I_1(t)$ and $I_2(t)$ are light intensities incident on the respective photomultipliers, and ΔI_1 and ΔI_2 are their fluctuations.

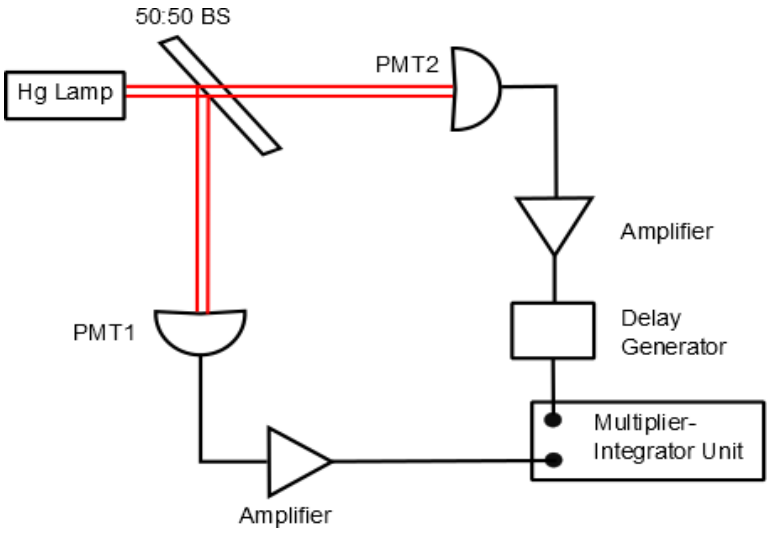

Fig 1: Diagram of HBT experiment involving intensity interferometer.

The fluctuations in the light intensity from the mercury discharge lamp are due to the fluctuations in the number of atoms emitting photons at a given time and occur on the timescale comparable to its coherence time, τ_c.

Coherence time is defined as the time interval over which the phase of the wave train remains stable, and is related to the line width or spectral width of the light source by the following relation[6]

$$\tau_c = \frac{1}{\Delta\omega} \tag{1.1}$$

where $\Delta\omega$ is the line width or spectral width of the light source.

The intensity fluctuations in each photomultiplier are correlated if light incident on the respective photomultiplier are within the coherence time.

The second order correlation function $g^{(2)}(\tau)$ is then defined as[6]

$$g^{(2)}(\tau) = \frac{\langle I(t)I(t+\tau)\rangle}{\langle I(t)\rangle\langle I(t+\tau)\rangle} \tag{1.2}$$

where $I(t)$ is the intensity of the light incident on the photomultipliers, τ is the time delay introduced and the angled brackets indicate time average.

The time-varying light intensity incident on the photomultipliers can be written as

$$I(t) = \langle I\rangle + \Delta I(t) \tag{1.3}$$

where $\langle I\rangle$ is the mean intensity of the light and $\Delta I(t)$ represents the fluctuations from the mean intensity.

For $\tau \ll \tau_c$, we expect the intensity fluctuations at times t and $t+\tau$ to be correlated and in particular for $\tau = 0$,

$$g^{(2)}(0) = \frac{\langle I(t)^2 \rangle}{\langle I(t) \rangle^2} \tag{1.4}$$

It follows from the Cauchy-Schwarz inequality that $\langle I(t) \rangle^2 \leq \langle I(t)^2 \rangle$, thus

$$g^{(2)}(0) \geq 1 \tag{1.5}$$

For coherent light, which is perfectly stable with no intensity fluctuations, $g^{(2)}(0)$ is equal to 1 and lasers are an example of such light. Bunched light consists of photons which tend to cluster or bunch together in timescales equivalent to their coherence time, has a $g^{(2)}(0)$ value that is greater than 1. Chaotic light from blackbodies is an example.

If we consider a Lorentzian broadened chaotic light, the $g^{(2)}(\tau)$ can be written as[6]

$$g^{(2)}(\tau) = 1 + e^{\frac{-2|\tau|}{\tau_c}} \tag{1.6}$$

with $g^{(2)}(0)=2$.

For $\tau \gg \tau_c$, we expect the intensity fluctuations at times t and $t + \tau$ to be completely uncorrelated.

$$\begin{aligned} \langle I(t)I(t+\tau) \rangle &= \langle \big(\langle I \rangle + \Delta I(t) \big) \big(\langle I \rangle + \Delta I(t+\tau) \big) \rangle \\ &= \langle I \rangle^2 + \langle I \rangle \langle \Delta I(t) \rangle + \langle I \rangle \langle \Delta I(t+\tau) \rangle \\ &\quad + \langle \Delta I(t) \rangle \langle \Delta I(t+\tau) \rangle \\ &= \langle I \rangle^2 \end{aligned} \tag{1.7}$$

where $\langle \Delta I(t) \rangle = 0$ by definition. Therefore, from Eqn 1.2 and 1.7,

$$g^{(2)}(\tau \gg \tau_c) = 1 \tag{1.8}$$

From Eqns 1.5 and 1.8, we observed that the $g^{(2)}(\tau)$ value peaks at $g^{(2)}(0)$ and decreases with larger values of τ to $g^{(2)}(\tau)=1$ for bunched light.

Since the intensity of light is proportional to the number of photons, the expression for $g^{(2)}(\tau)$ in Eqn 1.2 can be rewritten as the following if we consider a coincidence measurement

$$g^{(2)}(\tau) = \frac{\langle n_1(t) n_2(t+\tau) \rangle}{\langle n_1(t) \rangle \langle n_2(t+\tau) \rangle} \tag{1.9}$$

where $n_i(t)$ is the number of photons detected by detector i at time t. A coincidence measurement is a measurement of the time interval between consecutive detected photons in separate detectors. Such a measurement is done with a set-up identical to that in Figure 1, but with the amplifiers removed and the multiplier-integrator unit replaced with an oscilloscope which is able to record the time intervals.

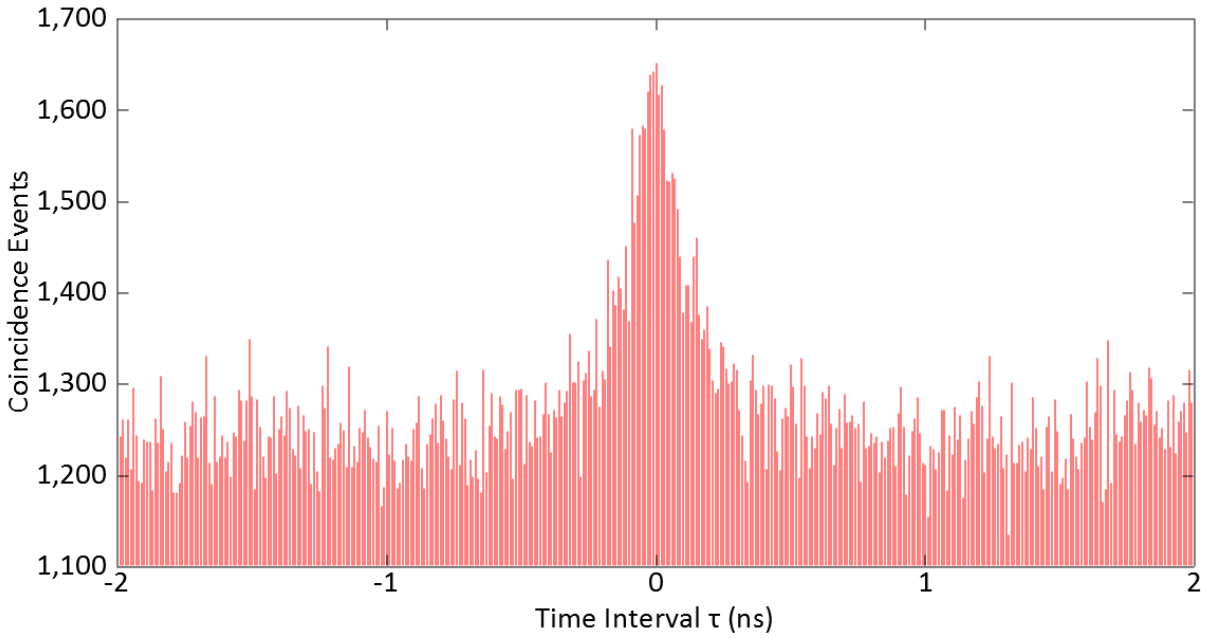

Fig 2: Coincidence measurement for bunched light with the photon bunching signal appearing between $\tau = \pm 0.5$ns and peaking at τ=0ns. This is expected as photons in bunched light are clustered in short time intervals and the probability of coincidence events decreases with time.

Eqn 1.9 can be interpreted as the conditional probability of detecting a photon in a photon detector at time $t = \tau$ given that a photon was detected in the other detector at time $t = 0$. In fact, the coincidence measurement is a $g^{(2)}(\tau)$ measurement. Figure 2 shows a typical coincidence measurement for bunched light displayed as a histogram in the oscilloscope.

In the quantum mechanical approach, for τ=0, Eqn 1.9 is expressed as[8]

$$g^{(2)}(0) = \frac{\langle \hat{n}_1 \hat{n}_2 \rangle}{\langle \hat{n}_1 \rangle \langle \hat{n}_2 \rangle} = \frac{\langle \hat{a}_1^+ \hat{a}_2^+ \hat{a}_2 \hat{a}_1 \rangle}{\langle \hat{a}_1^+ \hat{a}_1 \rangle \langle \hat{a}_2^+ \hat{a}_2 \rangle} \tag{1.10}$$

where $\hat{n} = \hat{a}^+ \hat{a}$ is the photon number operator, and $\hat{a}^+$ and $\hat{a}$ are the creation and annihilation operators respectively.

If we substitute $\hat{a}_1 = \frac{1}{\sqrt{2}}(\hat{a}_I - \hat{a}_V)$ and $\hat{a}_2 = \frac{1}{\sqrt{2}}(\hat{a}_I + \hat{a}_V)$, where $\hat{a}_I$ and $\hat{a}_V$ are the input and vacuum fields which enter the beamsplitter, Eqn 1.10 becomes[8]

$$g^{(2)}(0) = \frac{\langle \hat{n}_I (\hat{n}_I - 1) \rangle}{\langle \hat{n}_I \rangle^2} \tag{1.11}$$

Considering a nonclassical field state containing exactly one photon, we obtain $g^{(2)}(0)=0$ which violates the classical inequality of $g^{(2)}(0) \geq 1$ in Eqn 1.5. This is an example of nonclassical light known as antibunched light in which photons do not cluster together but tend to arrive one at a time. Antibunched light is produced by an individual emitting species such as an individual atom.

The $g^{(2)}(\tau)$ theoretical plots are shown in Figure 3. The photon bunching signal, $g^{(2)}(\tau)>1$, is the quantity that our project is aiming to increase, in the theoretical limit of 2 for blackbodies.

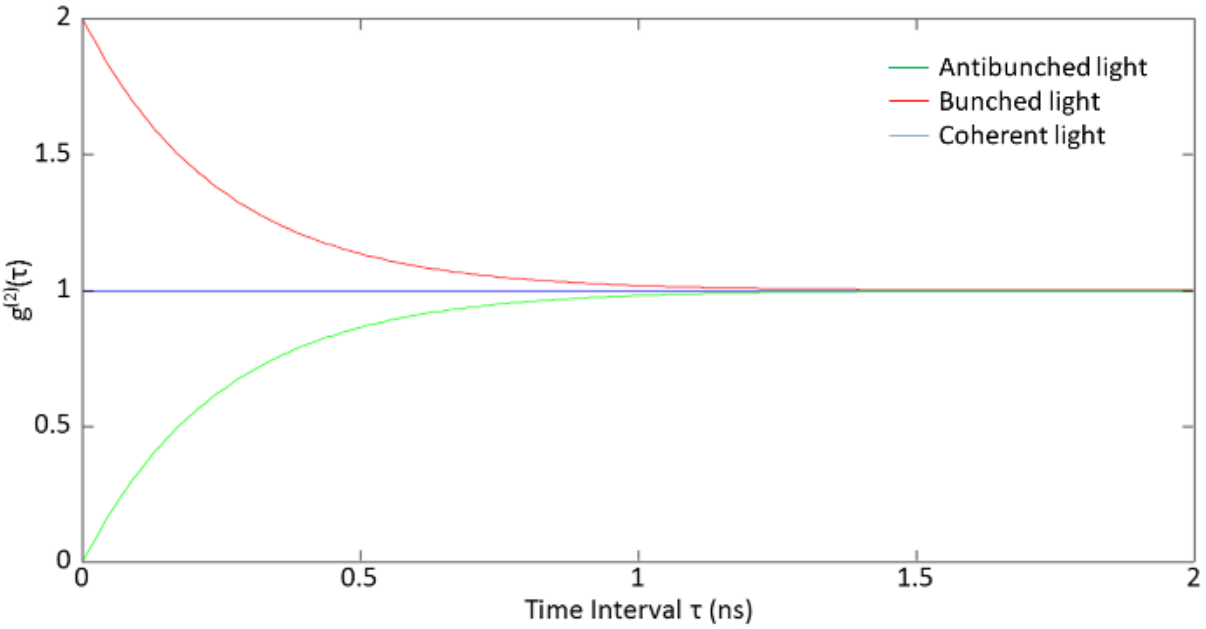

Fig 3: $g^{(2)}(\tau)$ theoretical plots for coherent, bunched and antibunched light.

Chapter 2

Methodology

2.1 Overview

The experimental set-up filters out a narrow band centred at 546.1nm from the spectrum of a light source to increase its coherence time (Eqn 1.1) such that our photon detectors are able to resolve the Lorentzian profile of the $g^{(2)}(\tau)$ measurement and obtain an increased photon bunching signal. 546.1nm light is used because the grating monochromator in the set-up is calibrated with a mercury discharge lamp and this wavelength corresponds to a transition with a strong line.

The filtering process is done in two stages using a grating monochromator and an etalon. The grating monochromator first narrows the bandwidth to approximately 0.1nm followed by the etalon which further narrows the bandwidth to 2pm. In doing so, the coherence time of the light source is increased from the order of 10fs to 0.5ns. This increased coherence time allows our photon detectors with 40ps resolution to resolve the profile of the $g^{(2)}(\tau)$ measurement.

The experiment was attempted on 3 light sources, namely a mercury discharge lamp, an arc lamp which simulates the spectrum of the sun, and the sun itself.

The experimental set-up comprises of 6 main components—the light source, a grating monochromator, an etalon, avalanche photon detectors, an oscilloscope, and a coelostat which focuses sunlight into a multi-mode fibre.

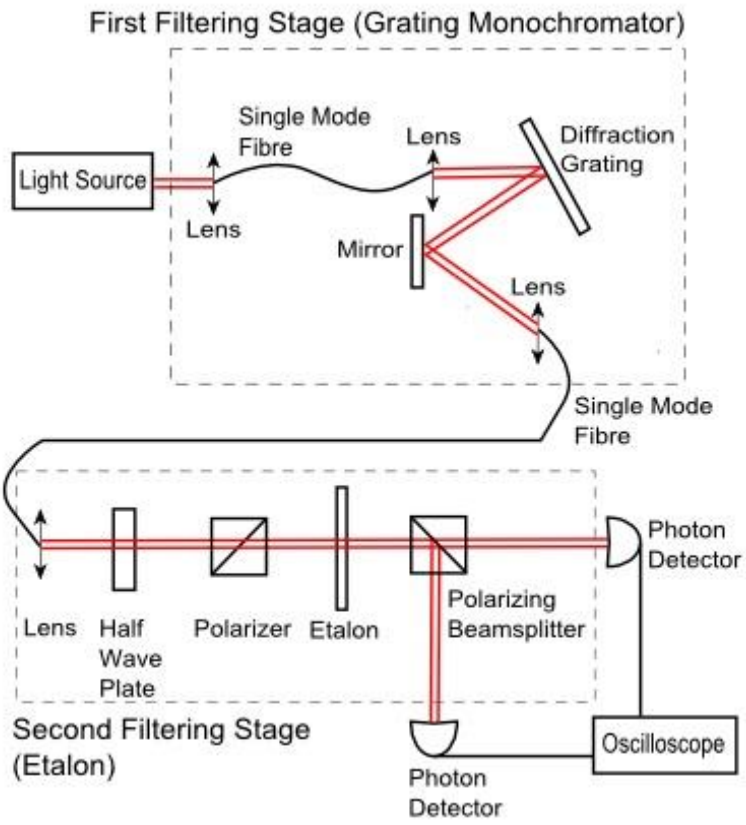

Fig 4: Diagram of the experimental set-up.

2.2 Light Sources

The light sources used for our experiment are a mercury discharge lamp, an arc lamp and the sun. The first two light sources are chosen specifically to lead up to the $g^{(2)}(\tau)$ measurement of the sun.

2.2.1 Mercury Discharge Lamp

The mercury discharge lamp has a discrete emission line spectrum with well-documented wavelengths (Fig 5), making it ideal for calibrating the grating monochromator. The 546.1nm line is chosen to calibrate the grating monochromator because it corresponds a strong line in the atomic transition ($5d^{10}6s7s\,^3S_1 \rightarrow 5d^{10}6s6p\,^3P^0_2$) of the Hg I (neutral Hg) spectrum and also because the peak wavelength from the sun is in the region of 500nm.

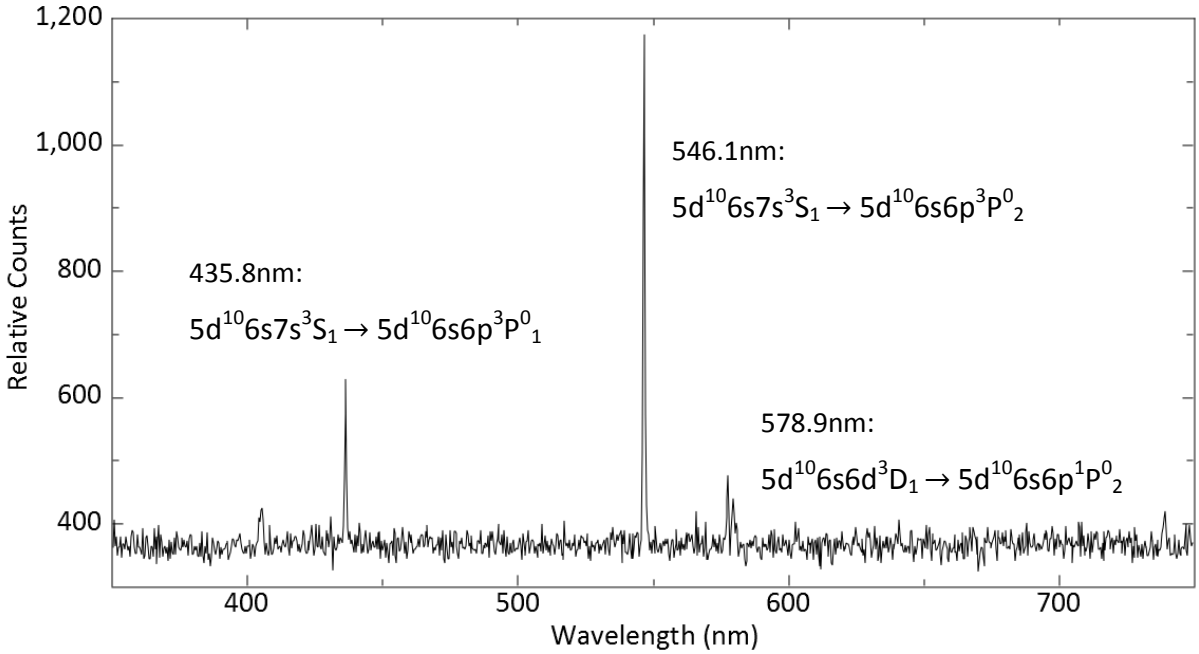

Fig 5: Spectral scan of mercury discharge lamp with a USB4000 Ocean Optics spectrometer.

2.2.2 Arc Lamp

The arc lamp is a Thorlabs High Power Light Source (HPLS-30-02). It is contained within a dielectric material which serves as an electric field concentrator to focus radio frequency energy into the lamp. Energy from the electric field rapidly heats the material in the bulb to a plasma state which emits a broadband spectrum of light (Fig 6). The plasma in the arc lamp contains argon and possibly traces of mercury which might explain the peak in the spectrum at 546nm.

The arc lamp is capable of reaching temperatures of approximately 6000K which is similar to that on the surface of the sun. Though a florescent lamp also produces a broadband spectrum, it only reaches a temperature of 3000K. By the Stefan-Boltzmann law, which states that the power emitted per unit area of the surface of a blackbody is directly proportional to the fourth power of its absolute temperature, the intensity of the florescent lamp is 16 times lower than that of the arc lamp. This lowered intensity translates to a significantly longer integration time for the $g^{(2)}(\tau)$ measurements which is not ideal.

These features of the arc lamp are useful as they allow us to simulate experiments for the $g^{(2)}(\tau)$ measurements of the sun, before performing actual measurements with the sun.

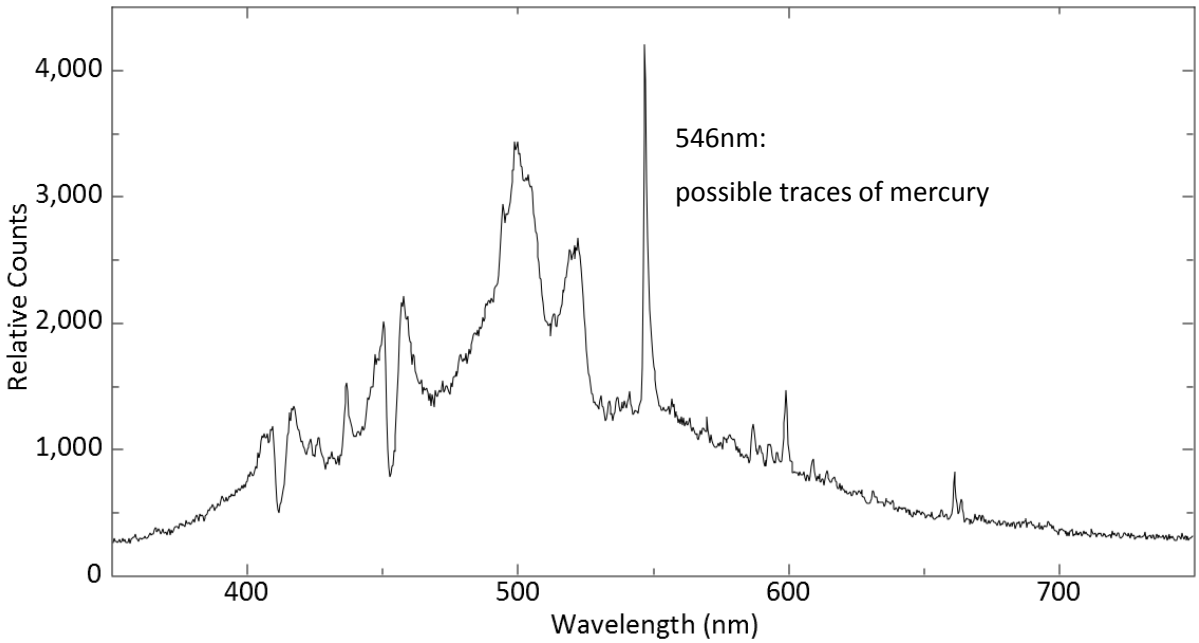

Fig 6: Spectral scan of arc lamp with a USB4000 Ocean Optics spectrometer.

2.2.3 Sun

Being the closest star to earth, the sun is the easiest celestial source to collect light from to conduct $g^{(2)}(\tau)$ measurements. It is a blackbody which produces a broadband spectrum of light with a peak wavelength in the region of 500nm (Fig 7).

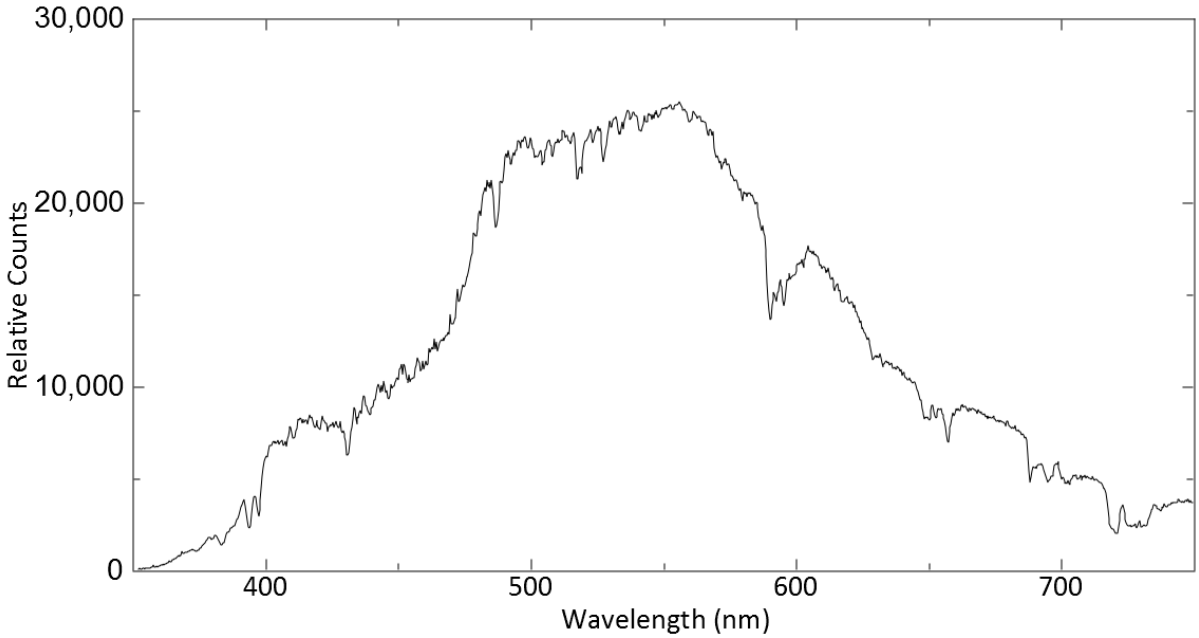

Fig 7: Spectral scan of the sun with a USB4000 Ocean Optics spectrometer.

2.3 First Filtering Stage (Grating Monochromator)

The purpose of setting up a grating monochromator, as opposed to using a fixed wavelength bandpass filter, is to provide the flexibility of filtering wavelengths of our choice across a broadband spectrum.

The grating monochromator consists of a diffraction grating, a motorized rotation stage on which the diffraction grating is mounted, 2 achromatic lenses and a mirror.

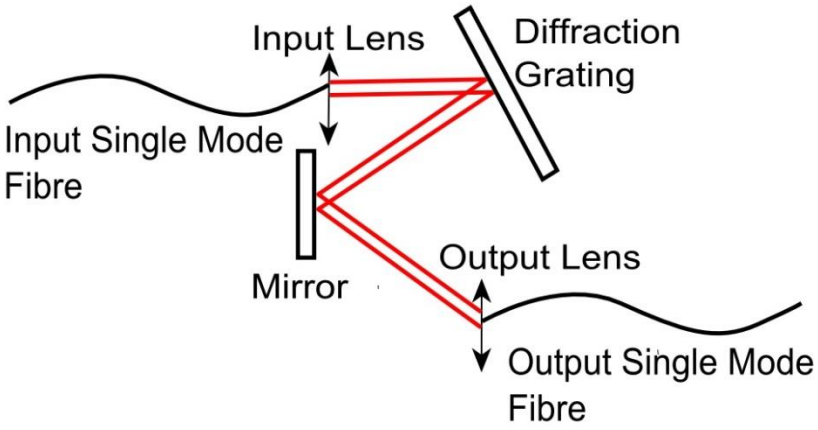

Fig 8(a): Diagram of grating monochromator.

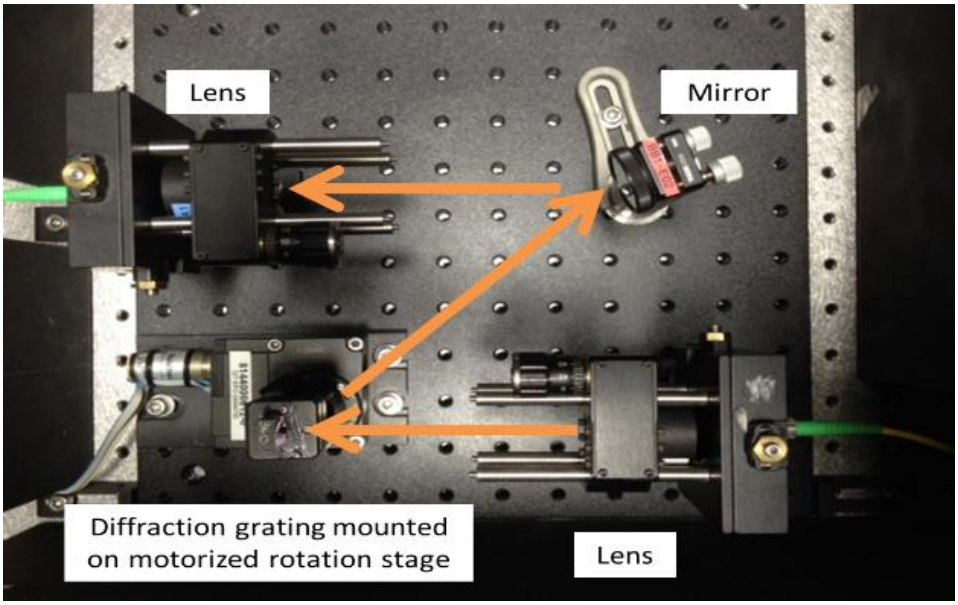

Fig 8(b): Top view of grating monochromator with beam path in orange.

2.3.1 Diffraction Grating

The purpose of the diffraction grating is to allow us to carry out spectral filtering. A ruled reflection grating is chosen over other types of gratings because of the higher efficiencies achieved through its blazed angles. The design of the ruled grating is such that approximately 70% of the diffracted beam is sent into the first order.

It is known that astigmatism varies with the square of the groove density of a grating and it results in a decrease coupling efficiency of light into a single mode fibre. Thus, given the available grating groove densities, the 1200 grooves/mm grating is chosen instead of the 1800 grooves/mm grating to reduce astigmatism.

2.3.2 Motorized Rotation Stage

A motorized rotation stage is used to rotate the grating with respect to the incident beam so that a particular wavelength of the first order diffraction can be reflected onto the mirror and collected in the output fibre. The grating is mounted on a tilt mount fixed onto the rotation stage.

The motorized rotation stage is controlled by a computer script which commands it to rotate in step sizes of 0.001°, corresponding to approximately 0.025nm in wavelength.

2.3.3 Achromatic Lens

The lenses in the grating monochromator are used to collimate light from the input fibre and to focus the diffracted beam from the grating into the output fibre.

In line with the objective of being able to select a particular wavelength from a broadband spectrum, achromatic lenses are chosen to reduce chromatic aberrations.

The achromatic lens before the grating is specifically selected such that the size of the collimated beam through the lens maximizes the resolving power of the grating. The resolving power of the grating is given by[9]

$$R = \frac{\lambda}{\Delta\lambda} = mN \tag{2.1}$$

where R is the resolving power of the grating, λ is the selected wavelength, $\Delta\lambda$ is the full width half maximum (FWHM) of the beam's transmission profile through the grating monochromator, m is the diffraction order and N is the number of grooves on the grating that are illuminated by the incident beam.

Thus, a large beam size is desirable, but the size of the incident collimated beam has to be smaller than the grating size of 12.7mm. To calculate the beam size, we use the following relation[9]

$$NA \approx \theta = \frac{D}{2f} \tag{2.2}$$

where NA=0.13 is the numerical aperture of the fibre, θ is the half-angle of the maximum cone of light that can enter or exit the fibre, D is the beam size and f is the focal length of the lens. The NA is described as the angle of acceptance for which light enters the fibre such that total internal reflection occurs within the core of the fibre.

The above calculation leads to the choice of an achromatic lens of 30mm focal length and a resultant beam size of 7.8mm.

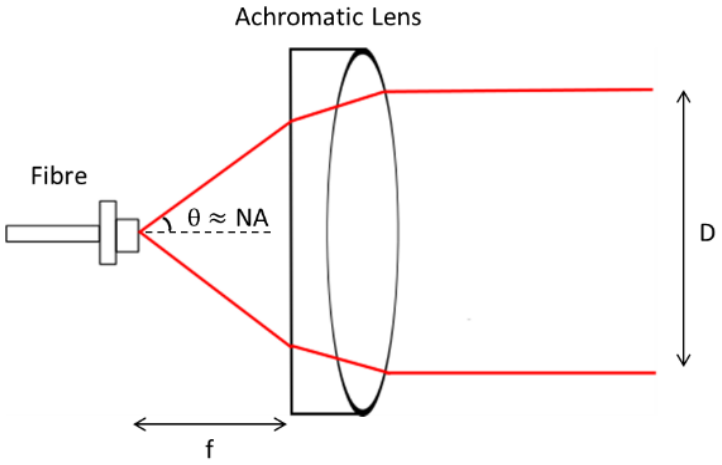

Fig 9: Illustration of the relation between θ, NA, D and f.

Having fixed the size of the collimated beam, as well as the NA of the fibre, the achromatic lens at the output end has to be identical to the input lens to maintain symmetry in the set-up.

As seen in Figure 10, the lenses are mounted on z-axis translation mounts. These mounts have adjustments screws with 50µm pitch for fine alignment in the z-axis over a range of 1.5mm. By convention, the z-axis is the axis of propagation of the beam of light. The mounts are in turn attached to cage rods to allow for rough positioning of the input and output lenses to collimate and focus the beam respectively.

In addition, the single mode fibres are attached to xy-axis translation mounts, which can be adjusted such that the input beam is incident on the centre of the input lens and the output beam focuses onto the core of the output fibre. These xy-axis translation mounts have adjustment screws with 0.25mm pitch for fine alignment over a range of 6mm.

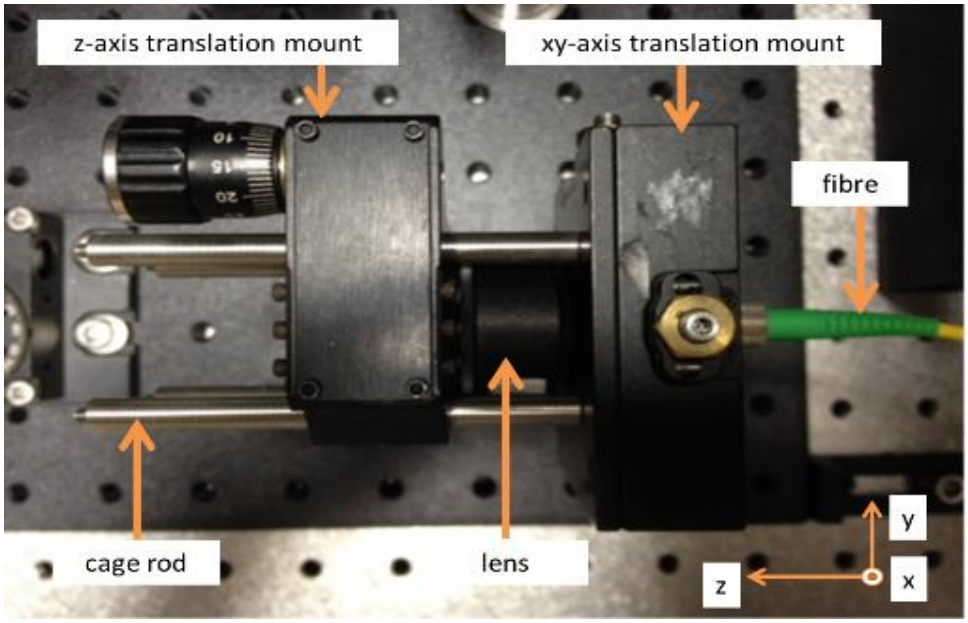

Fig 10(a): Top view of lens mount.

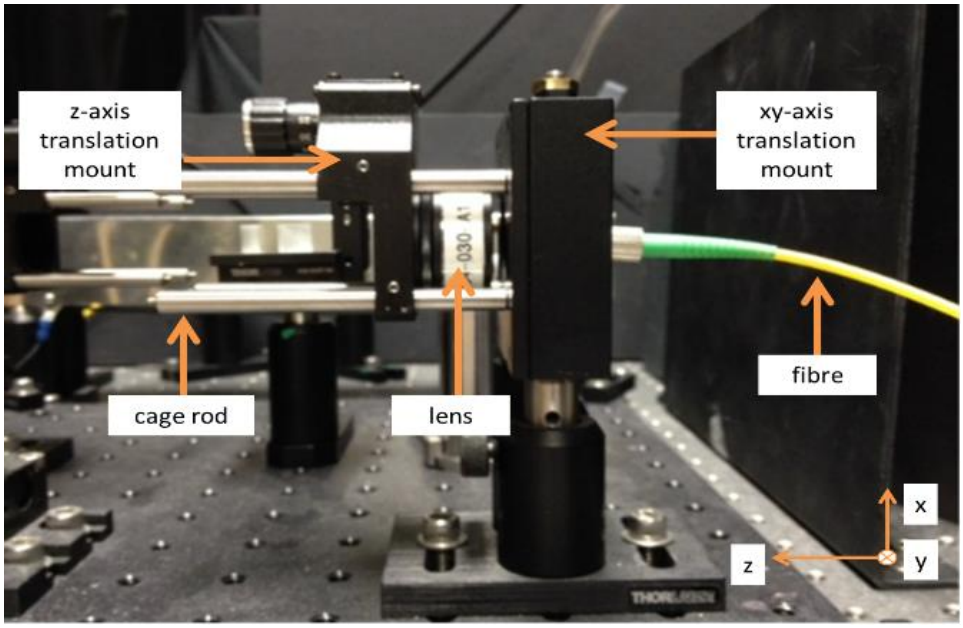

Fig 10(b): Side view of lens mount.

2.3.4 Mirror

A mirror with a coating of reflectivity greater than 99% over the visible spectrum is chosen to coincide with the grating monochromator's intended wavelength range. It is also attached to a mount which allows for tilt adjustments.

2.3.5 Alignment and Calibration Procedure

In the first stage of aligning the grating monochromator, a 25mW frequency-doubled Nd:YVO_4 laser beam of wavelength 532nm is sent in through both the input and output single mode fibres. The z-axis translation mounts are positioned along the cage rods to obtain approximately collimated beams. This green laser is used because it can be easily seen by the eye and is close to the wavelength used for the $g^{(2)}(\tau)$ measurements.

The green input beam is then aligned to the grating to ensure that the incident beam is not clipped by the edges of the grating. The grating is then rotated across various angles to check that the beam height remains constant since it is mounted on a tilt mount.

Next, a red laser beam is sent in through the output single mode fibre and the grating is rotated to an angle such that zeroth-order diffracted beam is incident on the mirror. We use the zeroth-order diffraction because diffraction does not occur and light behaves according to the law of reflection. This allows us to align the two beams of different wavelengths. Adjustments are made on both lens mounts and the mirror mount to ensure that the red and green lasers coincide at the same point on the diffraction grating, mirror, and both lenses.

The output single mode fibre is then coupled to a photon detector. Using the count rate as an indicator for the alignment, we further optimize the alignment by maximizing the count rate.

We then change the input source to a mercury discharge lamp because it of its well-defined 546.1nm spectral line. The grating is rotated to produce a first order diffracted beam that is incident on the mirror, and we re-optimize the alignment using the photon count rate by adjusting the lens mounts and mirror mount slightly to ensure that the input and output beams are collimated and optimally focused respectively.

Figure 11 shows the transmission profile of 546.1nm wavelength light from the mercury discharge lamp. The FWHM was found to be (0.122 ± 0.002)nm. The significance of this FWHM will be discussed in section 2.4.1.

Comparing the amount of light from the input and output fibres, we observe that the transmission efficiency of the grating monochromator is approximately 15%.

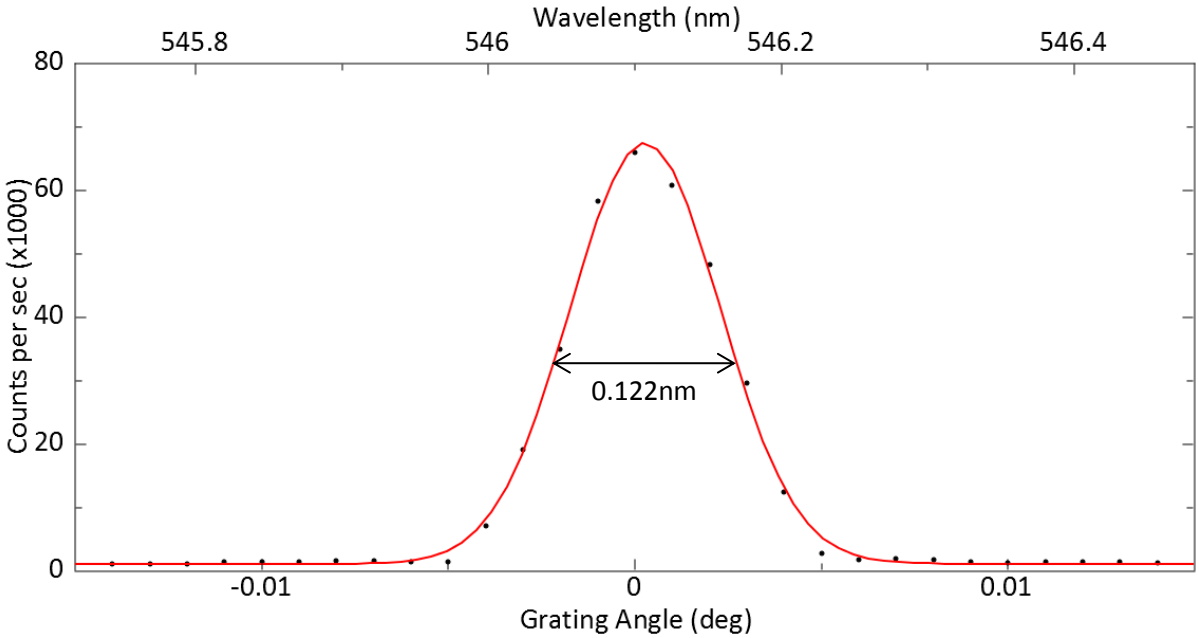

Fig 11: Transmission profile of 546.1nm light from mercury discharge lamp with (0.122±0.002)nm FWHM.

2.4 Second Filtering Stage (Etalon)

The etalon is used to further narrow the bandwidth of the source to 2pm so that the coherence time will be increased to 0.5ns, allowing the photon detectors to resolve the Lorentzian profile of the photon bunching signal. The physics of the narrowing process will be explained in section 2.4.1.

While the etalon is responsible for narrowing the bandwidth, other optical elements are necessary for coincidence measurements. These elements are a half wave plate (HWP), a Calcite Glan Taylor polarizer and a polarizing beamsplitter (PBS).

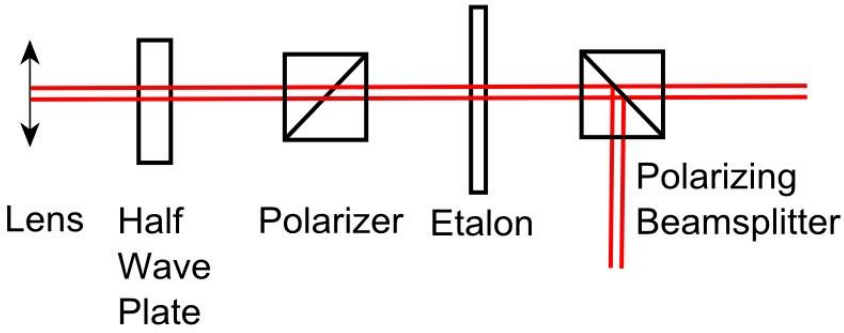

Fig 12(a): Diagram of the set-up at the second filtering stage.

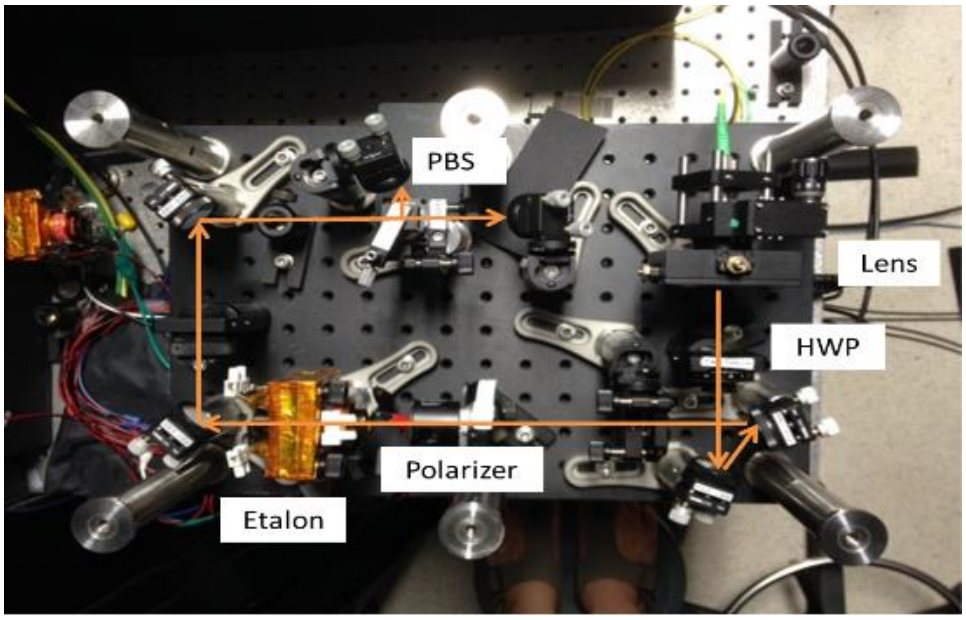

Fig 12(b): Top view of second filtering stage with beam path in orange.

2.4.1 Temperature-Tuned Etalon

The etalon is made of a single fused silica plate with two surfaces between which the incident beam undergoes multiple reflections. Through these reflections, constructive and destructive interferences occur to produce successive narrow transmission peaks (Fig 13).

The type of fused silica used for our etalon is a known as SUPRASIL®311. It is 25.4mm in diameter with a thickness, d, of 0.5mm. Its Free Spectral Range (FSR), the wavelength or

frequency spacing between each successive transmission peak, is approximately 0.205nm or 205GHz. The FSR is given by the following equation[10]

$$FSR = \frac{c}{2nd} \tag{2.3}$$

where c is the speed of light and n=1.46 is the refractive index of SUPRASIL®311.

Recalling from section 2.3.5, the grating monochromator selects a bandwidth of approximately 0.1nm. Thus, only one transmission peak will be selected when the grating monochromator is used together with the etalon. An illustration of this is shown in Figure 13. This was the motivation for aligning the grating monochromator to reduce the selected bandwidth to approximately 0.1nm.

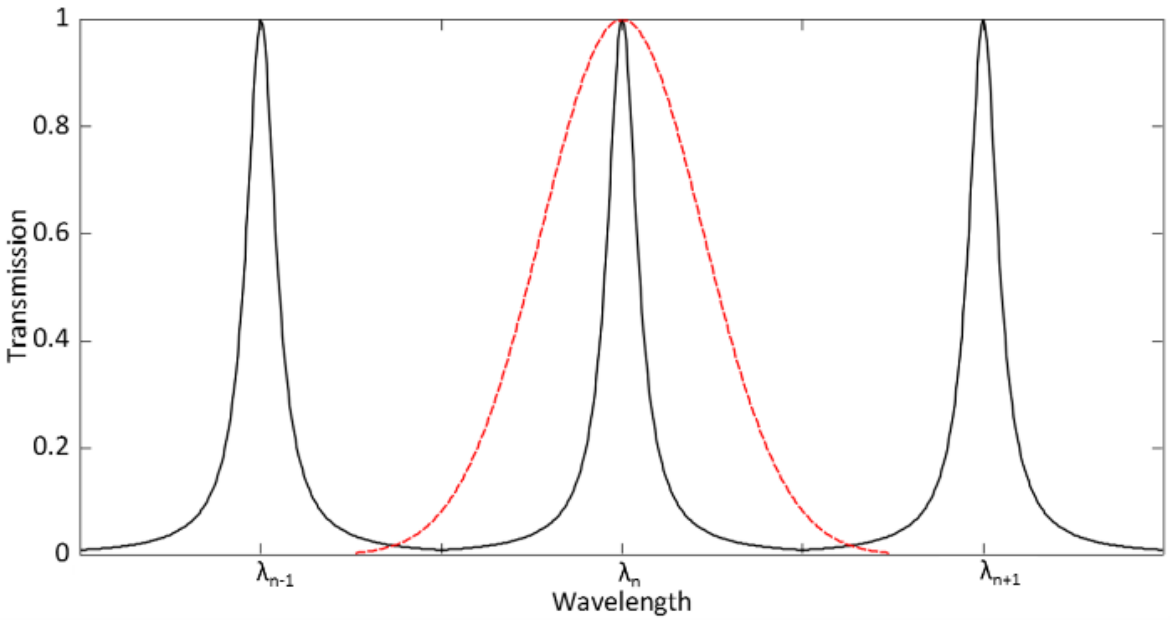

Fig 13: Illustration of the selection of a narrow band of wavelength centred on λ_n using the grating monochromator and etalon. The black solid line represents the transmission peaks of the etalon while the red dashed line represents the transmission through the grating monochromator.

The final transmission peak has a bandwidth of 2pm or 2GHz, and is determined by[9]

$$\frac{\pi\sqrt{R}}{1-R} \approx \frac{FSR}{\Delta\omega} \tag{2.4}$$

where R is the reflectivity of the etalon and $\Delta\omega$ is the bandwidth or FWHM of the transmitted peak. The etalon has a reflectivity of 97% over the range of 390nm to 810nm.

A temperature controller is connected to the etalon which allows us to tune the temperature to select the desired transmission peak. The tuning relation is approximately 5.1GHz/K. Its tuning relation can be calculated using[10]

$$\frac{\partial v}{\partial T} = \frac{c}{\lambda_0} \times \left(\frac{1}{n}\frac{\partial n}{\partial T} + \alpha\right) \tag{2.5}$$

where $\frac{\partial v}{\partial T}$ is the frequency shift per temperature change, λ_0 is the transmitted wavelength, $\frac{\partial n}{\partial T}$=1.28x10^{-5}/K is the temperature dispersion of SUPRASIL 311® and α=0.55x10^{-6}/K is the thermal expansion coefficient of SUPRASIL® 311.

With a temperature stability of $\pm$5mK over several hours, the controller ensures that the wavelength of the transmitted peak remains stable.

2.4.2 Half Wave Plate (HWP) and Calcite Glan Taylor Polarizer

The HWP and Calcite Glan Taylor polarizer are used in combination to maximize the count rates in the photon detectors.

A HWP with an anti-reflective (AR) coating for 546nm is used since the filtered narrow bandwidth is centred at that wavelength. The purpose of the HWP is to rotate the polarization of the incident beam to match the polarization set by the Calcite Glan Taylor polarizer.

The Calcite Glan Taylor polarizer is used to set the ratio of the vertical (V) and horizontal (H) polarizations of the incident beam so that the number of photons will be split equally at the polarizing beamsplitter. This is achieved by rotating the polarizer and observing the count rates of each photon detector after the beamsplitter.

2.4.3 Polarizing Beamsplitter (PBS)

A PBS is used to split the incident beam into two, transmitting V-polarized light while reflecting H-polarized light. Coincidence measurements can be done between the photon detectors on each output port of the PBS.

2.4.4 Alignment procedure

The alignment procedure for the etalon set-up is similar to that in section 2.3.5.

A green laser beam is first sent in through the input single mode fibre and the z-axis translation mount is positioned along the cage rods to obtain an approximately collimated beam.

A red laser beam is then sent in through the PBS in the opposite direction to the green laser beam. Adjustments to the etalon, the HWP, the polarizer and PBS are made to ensure that the beams are at normal incidence to their surfaces so that the optical path is not deflected when passing through these elements. The mirrors mounts are also adjusted to make sure that the green and red laser beams coincide at every point within these elements.

After a few iterations of this alignment process, the green input beam is coupled to output single mode fibres located at the end of each port of the PBS. The input beam is coupled using reflective collimators which have parabolic mirrors to focus the beam into the fibres. The other end of the output fibres are then coupled to photon detectors.

The HWP and polarizer are rotated to maximize and equalize the count rate in each detector. Minor adjustments are made to the mirror mounts and z-axis translation of the lens holder to further optimize the count rates.

2.5 Avalanche Photon Detectors (APDs)

APDs are single photons counters which operate by applying a bias above the breakdown voltage of special silicon photodiodes. The APDs remain in a metastable state and generate an avalanche upon photon detection.

It is important that the temporal resolution of the APDs is not larger than the coherence time of the photon bunching signal as this would reduce the strength of the signal[11]. Thus, in order to resolve the 0.5ns wide photon bunching signal, the temporal resolution of our APDs has to be smaller than 0.5ns.

We compare the jitter of two available APDs, namely the active quenching PDF from Micro Photon Devices (MPD) and the passive quenching C30902S from Perkin Elmer, with a Spontaneous Parametric Down Conversion (SPDC) source which generates photon pairs with a coherence time of 10ps. The photons from each pair are sent into separate APDs for coincidence measurements to quantify the jitter of the APDs.

Figure 14 shows the coincidence measurement results of the two different APDs. The jitter of the MPD and Perkin Elmer APDs are 40ps and 1.2ns respectively. This is because the Perkin Elmer APDs have a thicker silicon layer which makes the time for a photoelectron to reach the multiplier region more uncertain than in the thinner silicon layer of the MPD APDs.

Evidently, the MPD APDs have a much better temporal resolution than the Perkin Elmer APDs, and are capable of resolving the 0.5ns wide Lorentzian profile of the photon bunching signal.

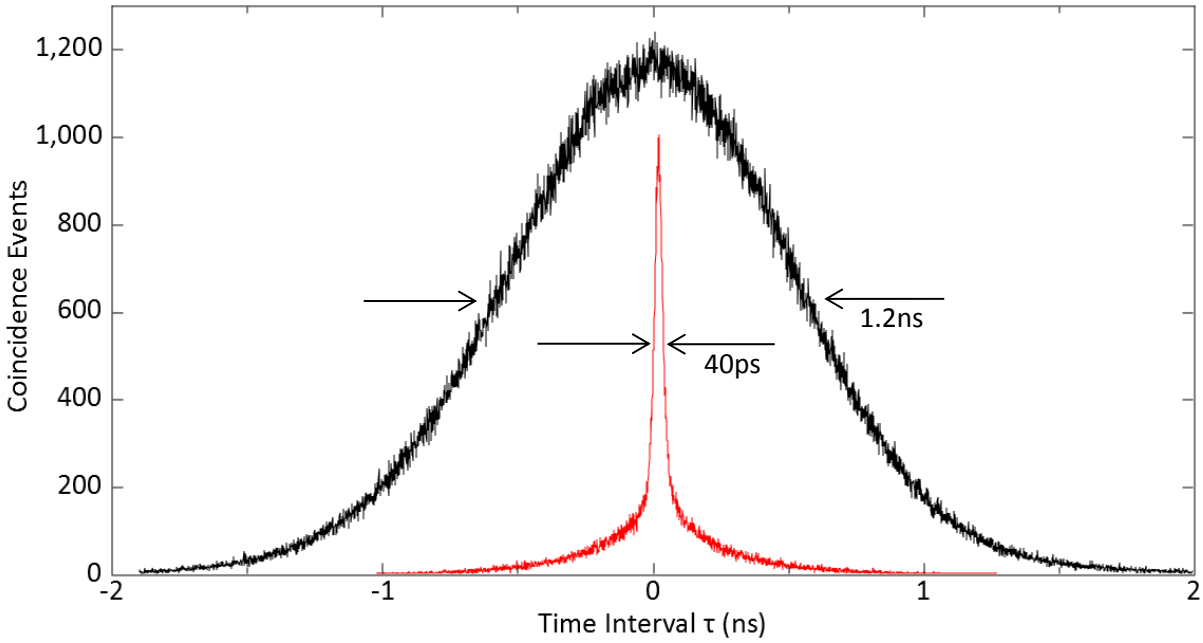

Fig 14: Coincidence measurements of photon pairs generated from SPDC using MPD (in red) and Perkin Elmer (in black) APDs.

2.6 Oscilloscope

The LeCroy WaveRunner 640Zi 4GHz Oscilloscope is connected to the MPD APDs and is used to record and display the coincidence measurements in a histogram (Fig 15). It has a timing uncertainty of less than 10ps which is determined by the interpolation of consecutive data points of a measurement.

The MPD APDs are connected to separate channels of the oscilloscope. One of the channels serves to arm the trigger for the measurement, while the other serves as a trigger to record the coincidence measurement.

The sampling mode used for the coincidence measurements is Sequencing. In this mode, the oscilloscope records 5000 events before processing the data and displaying the histogram of the coincidence measurements in that sample.

In comparison to Real Time sampling, which displays a coincidence measurement every time it measures one, the associated processing time for the coincidence measurements using Sequencing is approximately three orders smaller. This is due to the relatively high photon count rate in each APD. With a count rate on the order of 100k counts per second, continuous processing of the coincidence measurements using Real Time results in a significant amount of time needed to process the data. Therefore the effective dead-time using Real Time sampling is higher and also loses coincidence measurements.

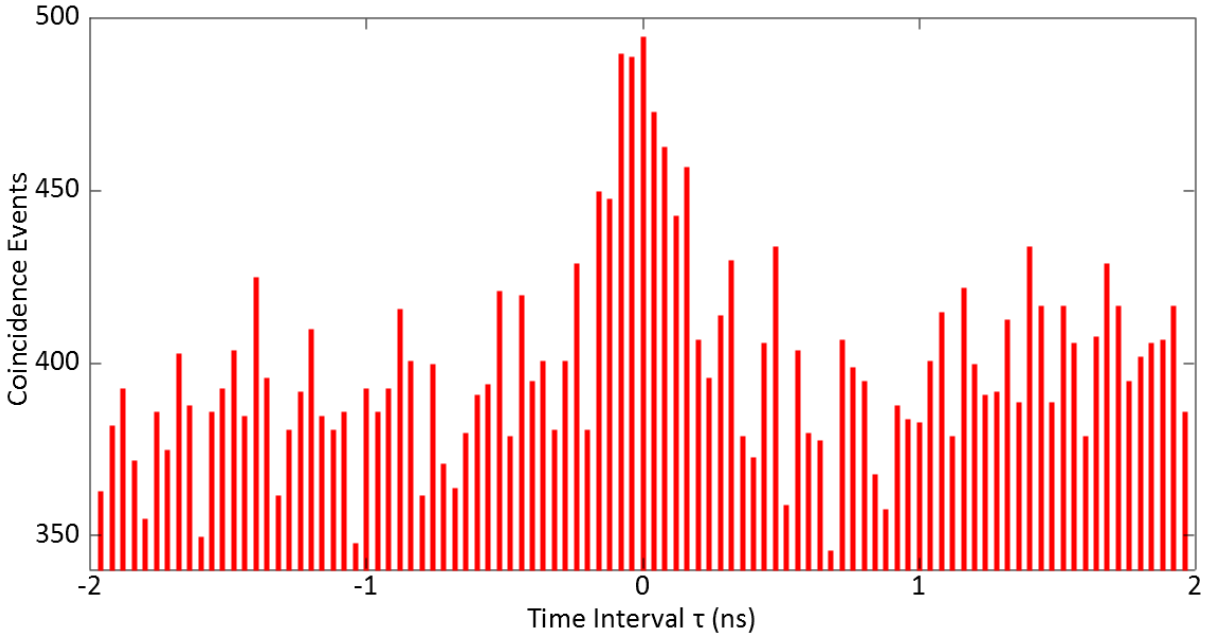

Fig 15: Oscilloscope displaying coincidence measurements as a histogram with 40ps time bin.

The time bin used for the histogram is chosen to be 40ps which corresponds to the temporal resolution of the APDs, while the total integration time for the coincidence measurements is on the order of hours.

2.7 Coelostat

A coelostat is an instrument which uses a mirror made to rotate at a constant rate around an axis parallel to the earth's rotation axis to reflect light from a portion of the sky into a fixed telescope[12].

We use a modified coelostat to couple sunlight to a multi-mode fibre (Fig 16a). It comprises of an aspheric lens, a mirror, a motorized rotation stage, and a controller to control the motorized rotation stage.

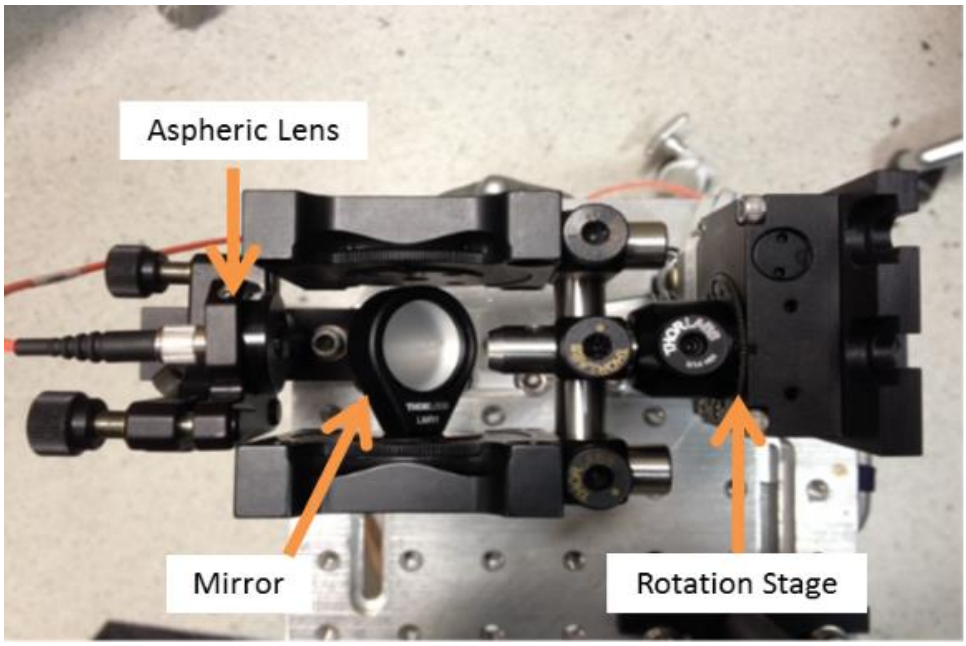

Fig 16(a): Top view of coelostat.

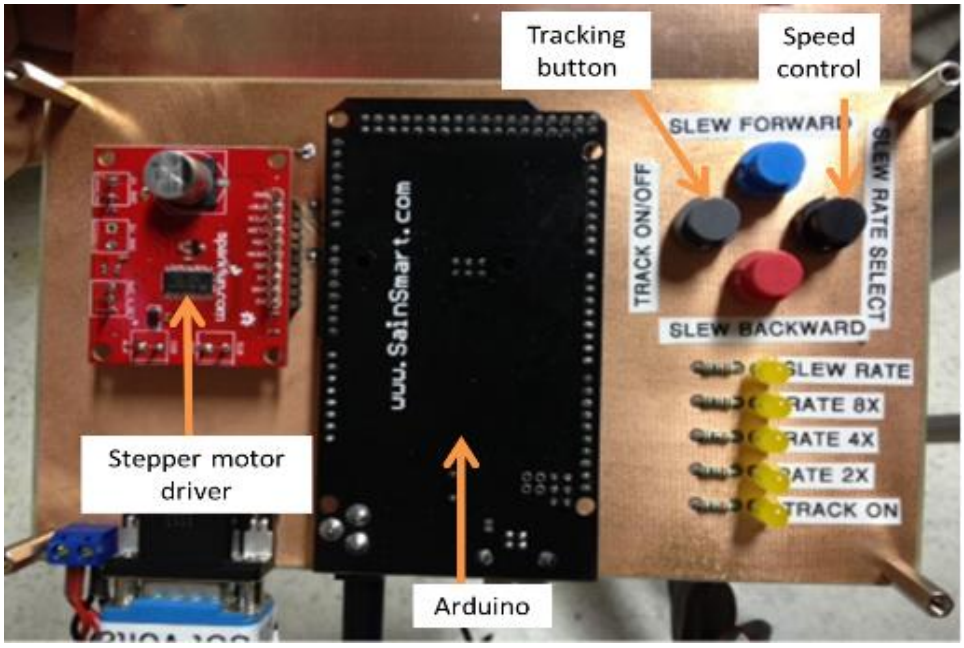

Fig 16(b): Image of the coelostat controller.

2.7.1 Aspheric Lens

An aspheric lens instead of a telescope is used to couple sunlight to the multi-mode fibre to make the set-up more compact and portable. The aspheric lens is fixed to a kinematic mount which allows tilt adjustments.

2.7.2 Mirror

The mirror is mounted to a motorized rotation stage which rotates the mirror such that the maximum amount of sunlight is directed towards the aspheric lens and multi-mode fibre.

2.7.3 Motorized Rotation Stage

The motorized rotation stage used in the coelostat is identical to that in section 2.3.2. It can be made to rotate at sidereal rate which is the rate of earth's rotation to track the motion of the sun across the sky.

2.7.4 Controller

The controller (Fig 16b) consists of an Arduino, a stepper motor driver, a manual speed control button and a tracking button.

An Arduino, a single-board microcontroller, controls the motorized rotation stage by instructing the stepper motor driver to move the rotation stage in a specified direction and rate for aligning and tracking purposes.

A manual speed control for the rotation of the motor is included to aid the alignment procedure. The faster rate of rotation corresponds to a rough alignment while the slower rate of rotation corresponds to a finer alignment.

The tracking button activates the motor to rotate at sidereal rate to track the sun.

2.7.5 Alignment Procedure

To track the sun and collect its light, the coelostat is placed on a tripod and positioned such that the axis of rotation of the mirror is aligned to North or parallel to the earth's rotation axis.

Following this, the multimode fibre from the coelostat is coupled to a power-meter to measure the optical power of the collected sunlight. We maximize the amount of sunlight coupled to the multi-mode fibre by adjusting the kinematic mount and rotating the mirror with the controller.

The power coupled to the multi-mode fibre is approximately 0.5mW on a clear day and approximately 50nW on a cloudy day. These values correspond to approximately 50k and 5 counts per second in the MPD APDs. It was found that the amount of sunlight that could be coupled to a multi-mode fibre was about 3 orders of magnitude more than through a single mode fibre.

Lastly, when the sunlight coupled to the multi-mode fibre is maximized, the tracking button is activated for the coelostat to track the sun.

Chapter 3

Results

3.1 Overview

Results of the $g^{(2)}(\tau)$ measurements for the mercury discharge lamp, arc lamp and the sun are shown in this chapter. In general, the experimental peak values of the $g^{(2)}(\tau)$ measurements or the photon bunching signals were less than the theoretical value of 2. However, these results are about a factor of 10 higher than what has been experimentally achieved so far for blackbody radiation. In addition, the measured coherence times were shorter than the theoretical coherence time of 0.5ns.

The equation of fit for the $g^{(2)}(\tau)$ measurements is

$$N(\tau) = f + s \times \left(1 + e^{\frac{-2|\tau|}{\tau_c}}\right) \qquad (3.1)$$

where $N(\tau)$ is the number of coincidence events measured by the oscilloscope, f is a term to account for the noise floor, s is a scaling factor for the Lorentzian profile of the $g^{(2)}(\tau)$ measurement, τ is the time interval between detected photons of each coincident event and τ_c is the coherence time.

The term $1 + e^{\frac{-2|\tau|}{\tau_c}}$ is the $g^{(2)}(\tau)$ for a Lorentzian broadened spectral line from a chaotic light source mentioned in Eqn 1.6.

The p-value is used to evaluate the fit to the data, with p=0.05 set as the significance level. This significance level implies that for any p-value less than or equal to 0.05, we reject the

hypothesis that the fit does not correspond to the data. The p-value is determined from the chi square (χ^2) per degree of freedom that the fit generates.

The evaluation of the results will be discussed in Chapter 4.

3.2 Mercury Discharge Lamp

The $g^{(2)}(\tau)$ measurement with the mercury discharge lamp was conducted over a period of 2 hours with a count rate of approximately 80k counts per second. The measurement produced a histogram with the expected Lorentzian profile (Fig 17).

The peak $g^{(2)}(\tau)$ value based on the fit was 1.64 ± 0.04 with a coherence time of (0.37 ± 0.01)ns. The p-value of the fit was 0.005 from the χ^2 per degree of freedom of 1.26.

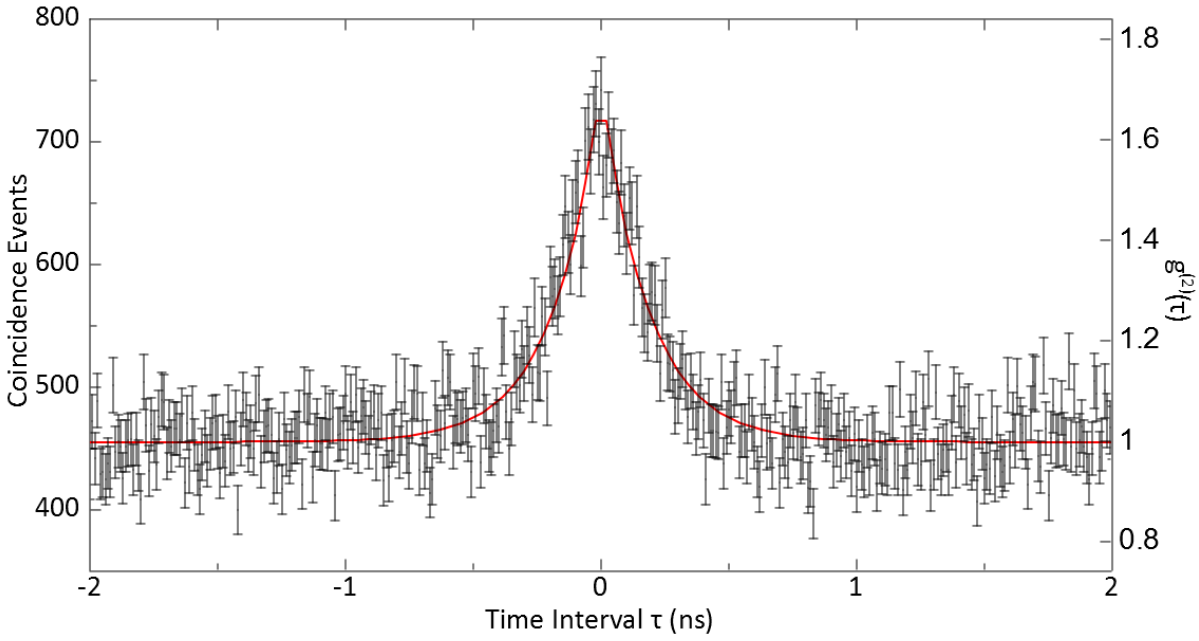

Fig 17: Results for the mercury discharge lamp with a peak $g^{(2)}(\tau)$ value of 1.64 ± 0.04 and coherence time of (0.37 ± 0.01)ns.

3.3 Arc Lamp

The $g^{(2)}(\tau)$ measurement with the arc lamp was conducted over a period of 2½ hours with a count rate of approximately 125k counts per second. As with the mercury discharge lamp, the measurement with the arc lamp produced a histogram with the expected Lorentzian profile (Fig 18).

The peak $g^{(2)}(\tau)$ value based on the fit was 1.35 ± 0.03 with a coherence time of (0.27 ± 0.01)ns. The p-value of the fit was 0.04 from the chi square per degree of freedom of 1.15.

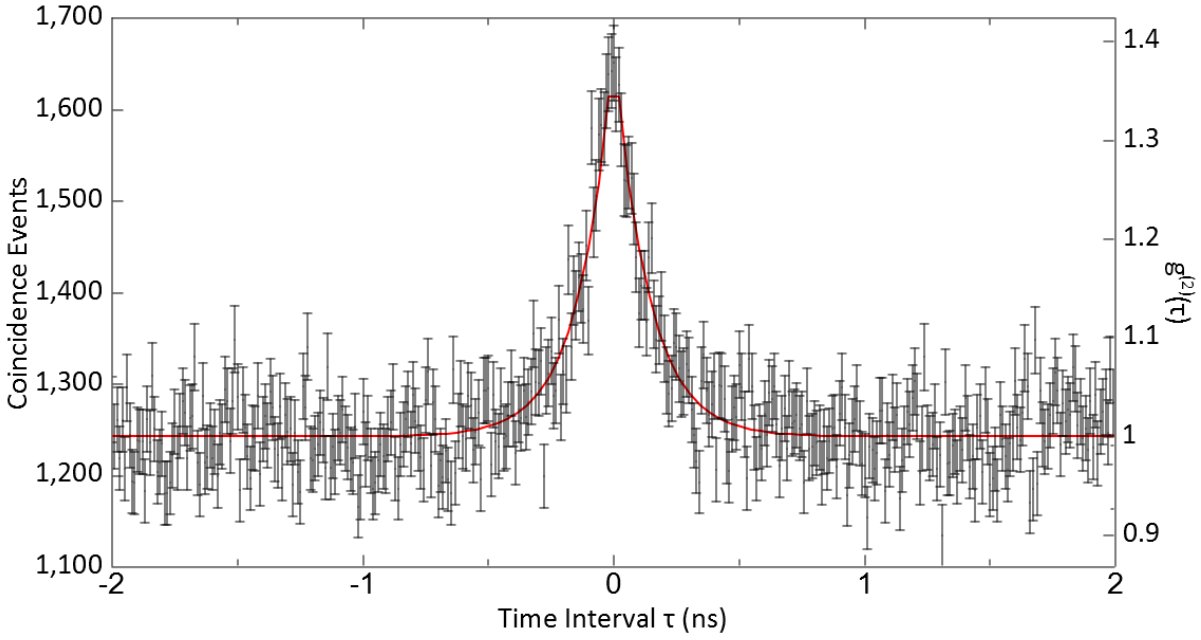

Fig 18: Results for the arc lamp with a peak $g^{(2)}(\tau)$ value of 1.35 ± 0.03 and coherence time of (0.27 ± 0.01)ns.

3.4 Sun

The $g^{(2)}(\tau)$ measurement with the sun was conducted over a period of 1 hour with a fluctuating count rate of approximately 125k counts per second. Unlike the mercury discharge lamp and arc lamp, the measurement with sun was subjected to weather

conditions such as the clouds and rain. Therefore, the integration time of the measurement was shorter compared to the other light sources. The measurement with the sun also produced a histogram with the expected Lorentzian profile (Fig 19).

The peak $g^{(2)}(\tau)$ value based on the fit was 1.31 ± 0.09 with a coherence time of (0.28 ± 0.05)ns. The p-value of the fit was 0.14 from the chi square per degree of freedom of 1.20.

The p-value for this measurement is higher than the significance value of 0.05 because the number of degrees of freedom is smaller than that of the mercury discharge lamp and the arc lamp. Still, the observed $g^{(2)}(\tau)$ measurement shows a convincing photon bunching signal.

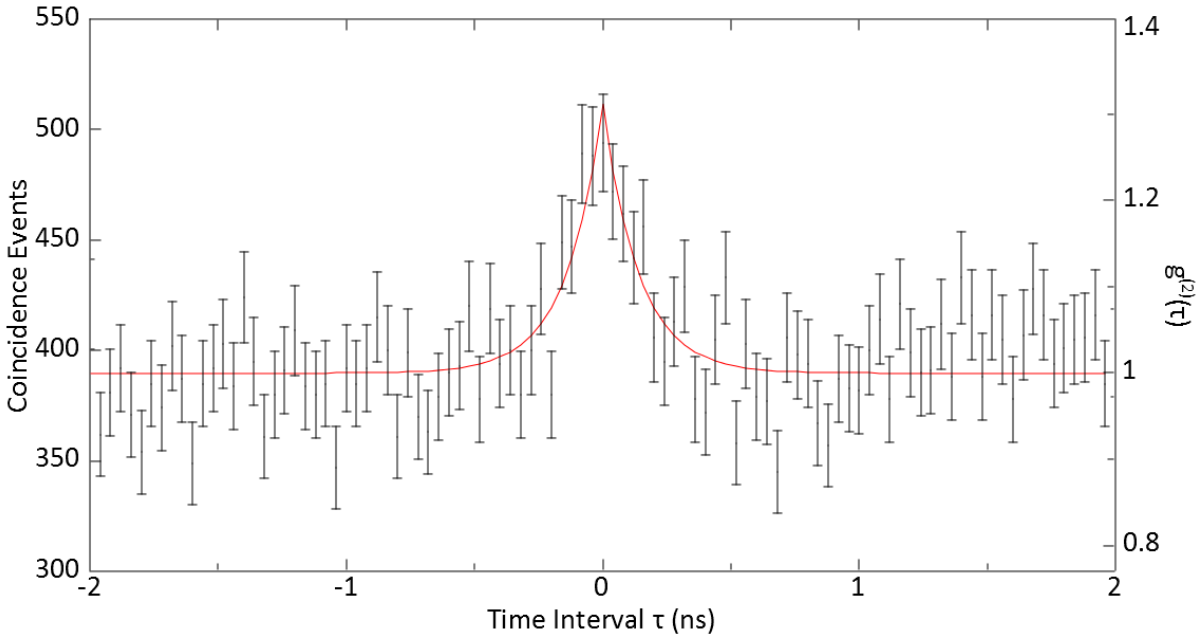

Fig 19: Results for sunlight with a peak $g^{(2)}(\tau)$ value of 1.31 ± 0.09 and coherence time of (0.28 ± 0.05)ns.

Chapter 4

Discussion

4.1 Overview

This chapter will cover the evaluation of the results in Chapter 3, how our set-up compares to what has been done and the possible experiments that can be done in future.

4.2 Evaluation of Results

As mentioned in section 3.1, the experimental peak values and coherence times of the $g^{(2)}(\tau)$ measurements were found to smaller than the theoretical values.

A few possibilities were raised as to why the experimental values were lower than expected. Firstly, the astigmatism associated with the use of a diffraction grating might have an effect on the $g^{(2)}(\tau)$ measurements. To test this hypothesis, the grating with 1200grooves/mm was replaced with a grating of 600grooves/mm since astigmatism improves with a decreased groove density.

While the light coupling efficiency into the collection fibre of the grating monochromator was tripled, the narrowest FWHM that was achieved with the 600grooves/mm grating was 0.23nm compared to 0.12nm with the 1200grooves/mm grating. This meant that a significant portion of the adjacent sidebands were transmitted in addition to the intended etalon transmission peak centred at 546.1nm (refer to Fig 13). A $g^{(2)}(\tau)$ measurement with the arc lamp now gave a lower peak $g^{(2)}(\tau)$ value of approximately 1.15 compared to the previously obtained 1.35.

A $g^{(2)}(\tau)$ measurement was then conducted with the mercury discharge lamp to verify whether the decrease in the peak $g^{(2)}(\tau)$ value to 1.15 for the arc lamp was due to astigmatism. We used the mercury discharge lamp because it only produces a single discrete emission line near the transmission peak of the etalon and is unaffected by high transmission of adjacent sidebands though the etalon. With a $g^{(2)}(\tau)$ peak value of approximately 1.6, similar to that obtained in section 3.2, it indicated that the decrease in the peak $g^{(2)}(\tau)$ value of the arc lamp was due to the sideband transmission through the etalon and not due to astigmatism.

With this understanding, we changed the grating to one with 1800grooves/mm to reduce the FWHM of the transmission through the grating monochromator and to further suppress the sidebands. However, because the astigmatism with the 1800grooves/mm diffraction grating was high, the light coupling efficiency into the collection fibre of the grating monochromator was only 0.25% compared to 26% with the 1200grooves/mm grating. A probable reason is that the mode selected by the input single mode fibre is changed due to the astigmatism caused by the grating. These changed modes do not match the mode needed to couple to the output single mode fibre, thus leading to the significant decrease in coupling efficiency. This lowered efficiency was not sufficient to couple enough light for a $g^{(2)}(\tau)$ measurement. Thus, it suggests that the current usage of the 1200grooves/mm is ideal.

This led to the other possibility that the extinction ratio of the etalon transmission, which is the ratio of the maximum to the minimum transmission through the etalon, was responsible for the lowered peak $g^{(2)}(\tau)$ value. To improve the extinction ratio, we decided to experiment with two identical etalons in series, instead of one etalon that was used originally, to suppress the tail ends of the transmission profile and result in a transmission peak with the sides of its profile falling sharply to zero as seen in Figure 13.

Using two 0.5mm thick etalons, the $g^{(2)}(\tau)$ measurements of the mercury discharge lamp and the arc lamp were conducted. For the mercury discharge lamp, the measured peak $g^{(2)}(\tau)$ value was 1.79 ± 0.01 while its coherence time was (0.47 ± 0.01)ns (Fig 20) compared to 1.64 ± 0.04 and (0.37 ± 0.01)ns with one etalon in the second filtering stage. For the arc lamp,

the measured peak $g^{(2)}(\tau)$ value was 1.52±0.04 while its coherence time was (0.42±0.02)ns (Fig 21) compared to 1.35±0.03 and (0.27±0.01)ns with one etalon in the second filtering stage. These results showed significant increments from previous measurements and thus proved that the poor extinction ratio of using a single etalon was partially responsible for the lowered peak $g^{(2)}(\tau)$ values and shorter coherence times.

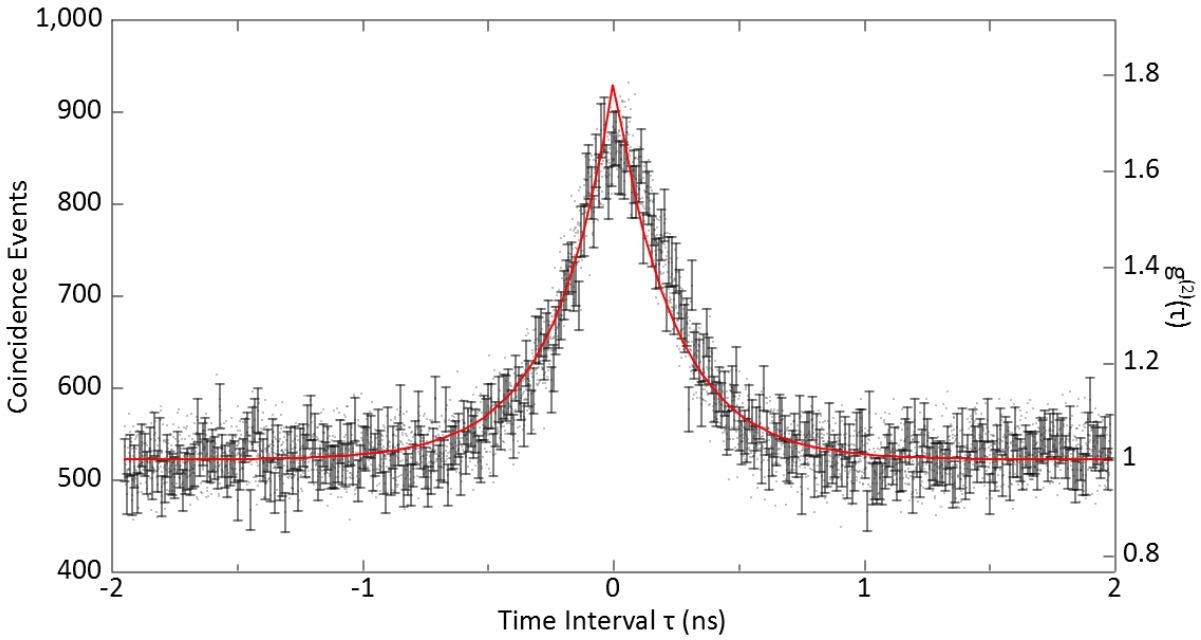

Fig 20: Results for the mercury discharge lamp with two 0.5mm thick etalons. A peak $g^{(2)}(\tau)$ value of 1.79±0.01 and coherence time of (0.47±0.01)ns were obtained.

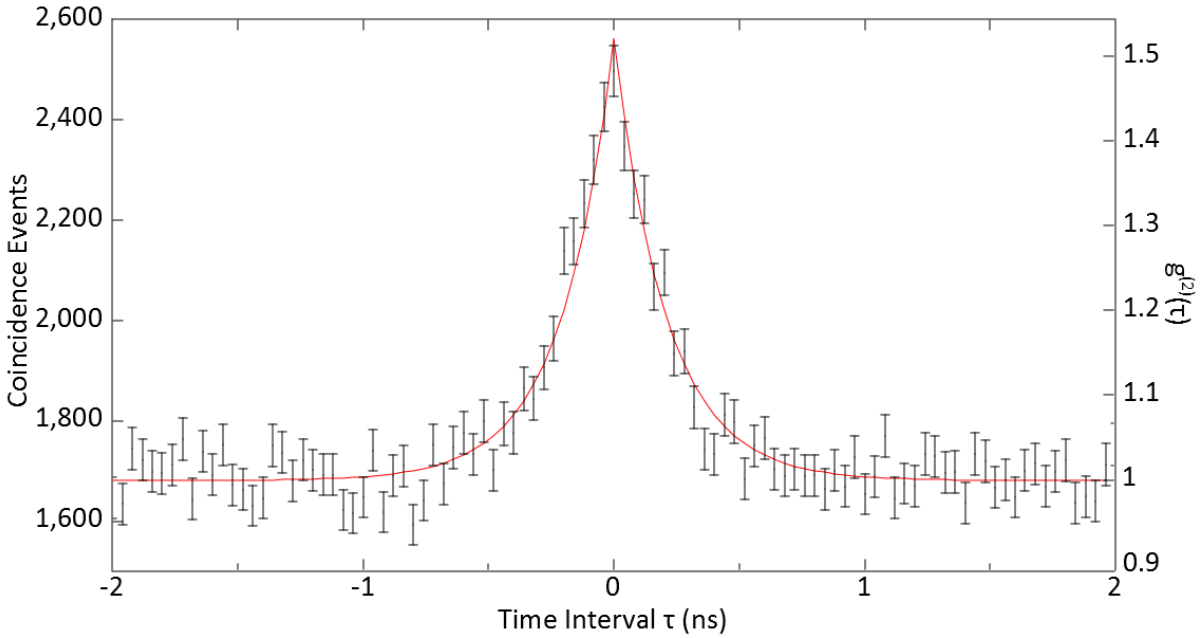

Fig 21: Results for the arc lamp with two 0.5mm thick etalons. A peak $g^{(2)}(\tau)$ value of 1.52 ± 0.04 and coherence time of (0.42 ± 0.02)ns were obtained.

Another possibility was the doubt over the temporal resolution of the MPD APDs. Observing Figure 14 carefully, we notice that the time interval between the tail-ends of the profile produced by the MPD APDs broadens to almost 1ns from 40ps at its FWHM. We hypothesized that the true resolution of the MPD APDs was larger than the 40ps previously claimed in section 2.5 and so they were unable to resolve the true peak of the $g^{(2)}(\tau)$ measurements.

To verify the maximum peak $g^{(2)}(\tau)$ value with the APDs, we used Mathematica to convolve the theoretical function of the $g^{(2)}(\tau)$ (Eqn 1.6) with a Lorentzian function of the form

$$\frac{\left(\frac{\omega}{2}\right)}{\pi\left(\tau^2+\left(\frac{\omega}{2}\right)^2\right)} \tag{4.1}$$

where ω is width of the Lorentzian function which we set to 40ps and τ is the time interval.

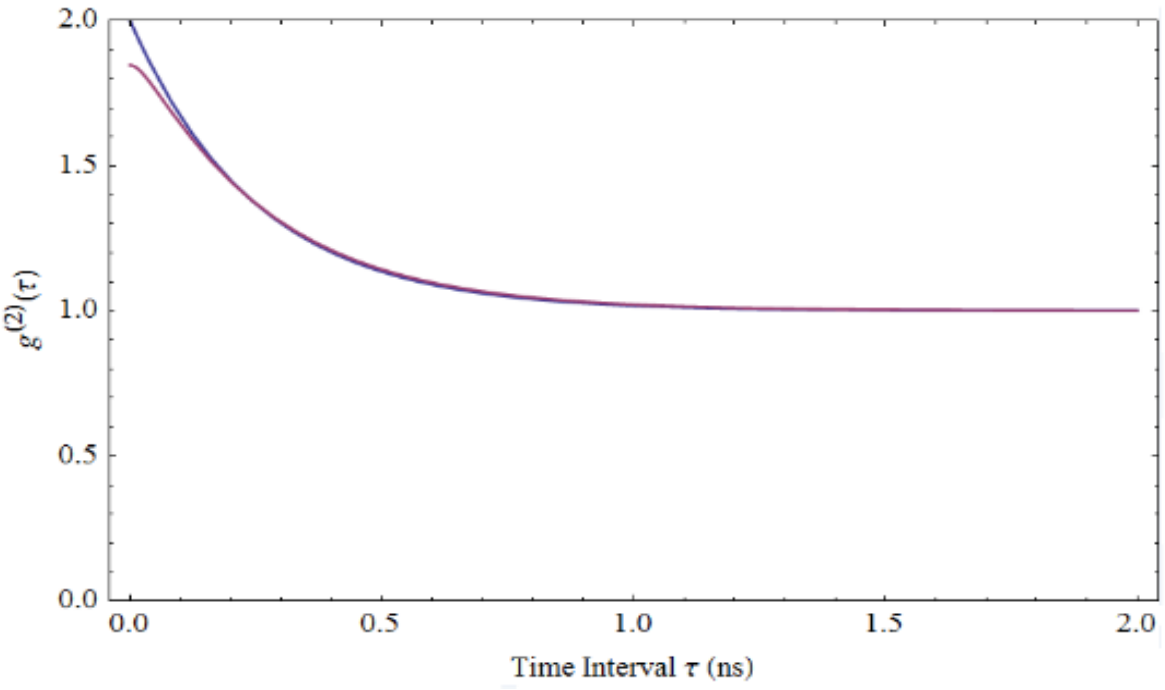

Fig 22: Plot of original $g^{(2)}(\tau)$ (in blue) and convolved function produced with MPD APDs (in purple).

The plot in Figure 22 shows that the convolution of the two functions lowers the peak $g^{(2)}(\tau)$ value to 1.85 from the original value of 2. This meant that the peak $g^{(2)}(\tau)$ value of 1.79 with the mercury discharge lamp and two etalons is very close to the new theoretical peak of 1.85.

However, it is still not known why the peak $g^{(2)}(\tau)$ value for the mercury discharge lamp is higher than that of the arc lamp and the sun. In other words, why is the peak $g^{(2)}(\tau)$ value for discrete emission lines higher than that of broadband light, given that the filtering process is identical in both cases?

4.3 Comparison of Set-Up

As a gauge of the how effective our experimental set-up is, we compare them to recent ones which are similar in design.

In an experiment for imaging polarimetry of the sun[13], two Fabry-Perot etalons and a grating spectrograph were used to filter and select wavelengths. The bandwidth that was achieved after filtering was 12pm, six times wider than the bandwidth through our set-up. This was due to the reflectivity of their etalons which was stated as 92.5%. While their purpose for filtering is different from ours, we have shown that it is possible to narrow a broadband spectrum to the order of 2pm.

A more recent experiment in February 2014[14] involved a similar set-up to ours which yielded a peak $g^{(2)}(\tau)$ value of 1.02 for the sun. The group filtered the sunlight to a bandwidth of 0.01nm which was one order of magnitude wider than ours and thus had a shorter coherence time for measuring the $g^{(2)}(\tau)$. Also, the temporal resolution of their photon detectors was 0.45ns, which was longer than their coherence time. The combination of short coherence time and insufficient resolution of the photon detectors led to the lower peak $g^{(2)}(\tau)$ value and thus weaker photon bunching signal compared to ours. Therefore, though our $g^{(2)}(\tau)$ measurements yielded peak values of 1.31 to 1.79, it is a significant step in realising the theoretical maximum value of 2 and a stronger bunching signal.

4.4 Future Work

Refinements to the extinction ratio of the etalon transmission have to be made to obtain the peak $g^{(2)}(\tau)$ value of 1.85. A possible next step after the refinements would be to conduct $g^{(2)}(\tau)$ measurements with other bright stars to determine their angular diameter.

Another possible experiment that can be done with the current set-up is to measure the linewidths of natural laser emissions, in particular from the stars Eta Carinae and Gamma Velorum A. These linewidths have not been spectrally resolved to date and are theoretically estimated to be on the order of 50MHz[15] or approximately 50fm.

Chapter 5

Conclusion

We have shown that the method of filtering a broadband spectrum of light from a blackbody can increase its coherence time by 4 orders of magnitude to almost 0.5ns to allow the photon detectors to resolve the Lorentzian profile of the $g^{(2)}(\tau)$ measurements and thus observe a strong photon bunching signal. After identifying the problems with the extinction ratio of the etalon transmission and resolution of the photon detectors, the experimental $g^{(2)}(\tau)$ peaks and coherence times obtained were in closer agreement to their respective theoretical values, and exceeded previously observed photon bunching signals by more than an order of magnitude.

It will be of interest to investigate the discrepancy between the peak $g^{(2)}(\tau)$ values of discrete emission lines and broadband light sources. In addition, further refinements to the extinction ratio of the etalon transmission will be made to improve the photon bunching signal. A confirmation of the linewidths of natural laser emissions is possible in the near future.

Bibliography

[1] Hanbury Brown, R. and Twiss, R. Q. *A New Type of Interferometer for Use in Radio Astronomy*. 1954, Philosophical Magazine, Vol 45. Pg 663-682.

[2] Hanbury Brown, R. *Measurement of Stellar Diameter*. 1968, Annual Review of Astronomy and Astrophysics, Vol 6. Pg 13-38.

[3] Hanbury Brown, R. and Twiss, R. Q. *A Test of a New Type of Stellar Interferometer on Sirius*. 1956, Nature, Vol 178. Pg 1046-1048.

[4] Gerry, C., and Knight, P. *Introductory Quantum Optics*. 2005, Cambridge University Press. Pg 4.

[5] Martienssen, W. and Spiller, E. *Coherence and Fluctuations in Light Beams*. 1964, American Journal of Physics, Vol 32. Pg 919-926.

[6] Fox, M. *Quantum Optics, An Introduction*. 2006, Oxford University Press. Pg 78-88, 105-120, 160.

[7] Hanbury Brown, R. and Twiss, R. Q. *Correlation Between Photons in Two Coherent Beams of Light*. 1956, Nature, Vol 177. Pg 27-29.

[8] Thorn, J. J., et al. *Observing the Quantum Behaviour of Light in an Undergraduate Laboratory*. 2004, American Journal of Physics, Vol 72. Pg 1210-1219.

[9] Lipson, S. G., et al. *Optical Physics*. 1995, Cambridge University Press. Pg 226, 251, 340.

[10] Doric, S. and Neron, J. *Application Note: Fabry-Perot Etalons*. 2005, Doric Lenses.

[11] Scarl, D. B. *Measurements of Photon Correlations in Partially Coherent Light*. 1968, Physical Review, Vol 175. Pg 1661-1668.

[12] Smart, W. M. *Textbook on Spherical Astronomy*. 1977, Cambridge University Press. Pg 225.

[13] Kleint, L. et al. *Combination of Two Fabry Perot Etalons and a Grating Spectrograph for Imaging Polarimetry of the Sun*. 2008, *Proc. SPIE* 7014, Ground-based and Airborne Instrumentation for Astronomy II, 701414 .

[14] Wu, L., et al. *Lensless Ghost Imaging with Sunlight*. 2014, Optics Letters.

[15] Dravins, D. and Germana, C. *Photon Correlation Spectroscopy for Observing Natural Lasers*. 2008, AIP Conference Proceedings. Vol 984. Pg 216-224